Applied Surface Science 505 (2020) 144584

Contents lists available at ScienceDirect

Applied Surface Science

journal homepage: www.elsevier.com/locate/apsusc

Full Length Article

Pre-ouzo effect derived fergusonite gadolinium ortho-niobate mesoporous nanospheroids for multimodal bioimaging and photodynamic therapy

Ganji Seeta Rama Raju[a], Eluri Pavitra[b], Hoomin Lee[b], Goli Nagaraju[c], Rengarajan Baskaran[d], Su Geun Yang[d], Cheol Hwan Kwak[b], Ganji Purnachandra Nagaraju[e,*], Yun Suk Huh[b,*], Young-Kyu Han[a,*]

[a] Department of Energy and Materials Engineering, Dongguk University–Seoul, Seoul 04620, Republic of Korea
[b] Department of Biological Engineering, Biohybrid Systems Research Center (BSRC), Inha University, Incheon 22212, Republic of Korea
[c] School of Chemistry, Centre for Research on Adaptive Nanostructures and Nanodevices (CRANN), Trinity College Dublin, Dublin 2, Ireland
[d] College of Medicine, Inha University, Chungsuk Bldg, Seohae-Daero, Chung, Incheon 22332, Republic of Korea
[e] Department of Hematology and Medical Oncology, Winship Cancer Institute, Emory University, Atlanta, GA 30322, United States

ARTICLE INFO

Keywords:
$GdNbO_4$ nanospheroids
Photoluminescence
Surface functionalization
Multimodal bioimaging
Photodynamic therapy

ABSTRACT

Rare-earth niobate compounds are excellent nonlinear optical materials. Unlike other niobate materials, gadolinium ortho-niobate ($GdNbO_4$) is reported to be inert in the visible region. The synthesis of pure-phase $GdNbO_4$ with a definite morphology suitable for biomedical applications is still a great challenge. In this study, a novel strategy is introduced to successfully facilitate the bioavailability of $GdNbO_4:Eu^{3+}$ luminescent material by harnessing the pre-ouzo effect during the synthesis of mesoporous $GdNbO_4:Eu^{3+}$ nanospheroids. Because of the materialization of $GdNbO_4$ nanodomains, the mesoporous $GdNbO_4$ nanospheroids exhibit paramagnetic behaviour and allows the strong broadband excitation between 300 and 500 nm, which permits NbO_6 emissions to be obtained in the visible region, whereas Eu^{3+} activated mesoporous $GdNbO_4$ nanospheroids produce an intense red emission under UV, near-UV and visible excitations. These mesoporous nanospheroids also demonstrate excellent cellular internalization for HCT116 and SW680 colon cancer cells and work in conjunction with optical and magnetic resonance imaging for the accurate diagnosis and prognosis of anatomical and physiological functions. The conjugation of chlorin e6 with mesoporous $GdNbO_4:Eu^{3+}$ nanospheroids leads to efficient photodynamic therapy (PDT) in cancer treatment. Ultimately, our approach represents an advance in the use of mesoporous $GdNbO_4:Eu^{3+}$ nanospheroids as multifunctional nanoprobes for multimodal imaging and PDT.

1. Introduction

Molecular imaging technologies such as computed tomography, nuclear imaging, optical imaging, positron emission tomography, and magnetic resonance imaging (MRI) have emerged as promising tools for clinical diagnosis [1–6]. Significant progress has been made in developing and refining these imaging modalities, but each individual imaging technology faces limitations in terms of the information it can provide for disease diagnosis and tumor detection [7]. For example, optical imaging provides cellular- or molecular-level information that is highly sensitive with a high spatial resolution, but the penetration depth is too limited for anatomical and physiological details to be discerned [8]. In contrast, as a noninvasive imaging technology, MRI provides extremely high spatial and temporal resolution for anatomical information but suffers from insufficient sensitivity and low planar resolution [6,8]. Therefore, recent research has focused on the development of multimodal imaging materials to bridge the gap in terms of resolution and sensitivity between these two imaging modalities. These dual-modalities allow synergistic information to be collected for the effective and accurate diagnosis and prognosis of anatomical and physiological functions by providing 3D anatomical images with high spatial resolution, deep penetration, and high sensitivity [9–11].

In order to combine MRI and optical imaging, any imaging probe used should possess paramagnetic or super-paramagnetic characteristics and superior luminescent properties [12]. Most MRI and optical dual-modal imaging probes utilize inorganic nanomaterials based on rare-earth (RE) elements due to their promising optical properties, with a large Stokes shift, and their magnetic behavior, which are associated with their outer-shell f-electrons [13–19]. In particular, gadolinium-based nanomaterials have been widely investigated as dual-modal

---

* Corresponding authors.
E-mail addresses: pganji@emory.edu (G.P. Nagaraju), yunsuk.huh@inha.ac.kr (Y.S. Huh), ykenergy@dongguk.edu (Y.-K. Han).

https://doi.org/10.1016/j.apsusc.2019.144584
Received 5 August 2019; Received in revised form 31 October 2019; Accepted 1 November 2019

imaging probes due to their excellent paramagnetic behavior, which is promising as a T1 contrast agent for MRI, and the ability to exhibit Stokes and anti-Stokes fluorescence by accommodating other trivalent RE activator ions such as Eu^{3+}, Tb^{3+}, Dy^{3+}, Er^{3+}, and Yb^{3+} [15,20–23]. For example, Saha et al. [17] reported the use of Eu^{3+} ion doped Gd_2O_3 nanoplates as a dual-imaging probe by exhibiting T1 MRI and Stokes fluorescence-based optical imaging. Ma et al. [24] reported $NaGdF_4:Yb^{3+}/Er^{3+}@NaGdF_4:Nd^{3+}$ core-shell nanostructures for T1 MRI and anti-Stokes fluorescence-based optical imaging. The main advantage of the Gd-based nanoparticle systems over Gd-chelates is that Gd-based nanoparticles exhibit less leakage of Gd ions and greater relaxivity due to the availability and higher density of magnetic ions [25]. However, currently developed Gd-based dual-imaging probes require a complicated synthesis process to obtain enhanced luminescent properties and also require surface functionalization to lower their toxicity, gain the desired zeta potential, and enhance cellular internalization [26,27]. Gd-based nanomaterials also exhibit limited excitation light harvesting ability and limited wavelengths with sharp bands [17,26]. Therefore, it is necessary to develop novel Gd-based nanomaterials with broadband excitation, enhanced luminescence properties, lower toxicity, and higher cellular internalization, in addition to carrying the photosensitizing anticancer drugs for photodynamic therapy (PDT). This is because the PDT is emerging as an alternative to chemo- and radiotherapy for cancer treatment [28].

$RENbO_4$ compounds with a fergusonite monoclinic structure have attracted attention due to their advantageous physicochemical properties such as low phonon frequencies, self-activating luminescence, greater dielectric constants and nonlinear optical properties. Among the $RENbO_4$ compounds, $GdNbO_4$ is an essentially inert material in the visible region under UV light excitation due to the efficient energy transfer from its NbO_6 octahedral units to the Gd^{3+} ions. However, $GdNbO_4$ is still a promising host material for doping with trivalent RE ions owing to their chemical stabilization and Gd^{3+} sensitization effects. Liu et al. [29] studied $GdNbO_4:Ln^{3+}$ nanocrystalline phosphors using a pechini-type sol-gel process for light-emitting diodes and field-emission display applications. Yang et al. [30] developed $GdNbO_4:Ln^{3+}$ single crystals using a high-temperature, high-pressure hydrothermal reaction for solid-state lighting applications, while the pressure- and temperature-induced luminescence properties of $GdNbO_4:Eu^{3+}$ were investigated by Hou et al. [31]. However, all of these investigations focused on solid-state lighting applications. Even though several studies have investigated the bioavailability of Gd- and Nb-based oxide nanomaterials, research on the biomedical applications of $GdNbO_4:RE^{3+}$ has yet to be conducted, possibly due to the appearance of intense excitation that is limited to the deep UV region, i.e. UV-C (200–300 nm), and also because of the lack of a suitable morphology. Indeed, the development of an appropriate morphology with a non-toxic nature and that enhances the absorption of excited photons in the near-UV (NUV) and visible regions remains a challenge and currently limits the use of $GdNbO_4:RE^{3+}$ in biomedical applications.

Among different synthesis techniques, the surfactant-free approach for the synthesis of inorganic nanoparticles has gained abundant interest due to its robust and facile synthesis protocols with nontoxic solvents, limited organic impurities, virtuous accessibility of the nanoparticles surface, environmentally friendly, and scale-up potential [32–37]. Besides, for the development of mesoporous inorganic nanoparticles, organic templates have been used in the surfactant-free synthesis but the removal of templates using the calcination or chemical extraction may affect the surface properties of the nanoparticles [38–40]. Therefore, in this study, we introduce a novel strategy for the development of mesoporous $GdNbO_4:Eu^{3+}$ nanospheroids for use in biomedical applications via the self-assembly of $GdNbO_4:Eu^{3+}$ nanodomains. Ethylenediaminetetraacetic acid (EDTA) plays dual role as a complexing and capping agent, which inhibits to a certain extent Ostwald's ripening process during the growth stage. The pre-ouzo effect produces the surfactant-free micelles in the growth solution, and these micelles facilitate the self-assembly of EDTA-capped $GdNbO_4:Eu^{3+}$ nanodomains to form mesoporous $GdNbO_4:Eu^{3+}$ nanospheroids. These mesoporous $GdNbO_4:Eu^{3+}$ nanospheroids have significant potential for use in the optical and MRI dual-modal imaging of colon cancer cells. Photosensitizer chlorin e6 (Ce6) and folic acid (FA-)conjugated $GdNbO_4:Eu^{3+}$ nanospheroids ($GdNbO_4:Eu^{3+}$@Ce6@FA) are also examined for their use in PDT in cancer treatment.

2. Experimental

2.1. Synthesis of mesoporous $GdNbO_4:Eu^{3+}$ nanospheroids

$GdNbO_4$ and $Gd_{(1\text{-}0.05)}NbO_4:0.05Eu^{3+}$ spheroid like nanostructures were prepared using the hydrothermal synthesis process that employed stoichiometric amounts of gadolinium nitrate hexahydrate [$Gd(NO_3)_3{\cdot}6H_2O$], europium nitrate pentahydrate [$Eu(NO_3)_3{\cdot}5H_2O$], niobium chloride ($NbCl_5$), and EDTA. For the synthesis, Gd- and Nb-based solutions were prepared separately. Solution I was prepared by dissolving 0.643 g of $Gd(NO_3)_3{\cdot}6H_2O$, 0.032 g of $Eu(NO_3)_3{\cdot}5H_2O$, and 0.012 g of EDTA in 65 ml of DI water and heating the solution to 70 °C under continuous magnetic stirring to form a chelated $Gd_{0.95}Eu_{0.05}$ complex. Solution II was prepared by dissolving 0.135 g of $NbCl_5$ in 10 ml of isopropanol, sonicating for 5 min, and then stirring until a homogeneous solution was formed. Solution II was then added dropwise to Solution I and stirred continuously for 2 h. This milky-white solution was then transferred to a Teflon liner (120 cm^3 volume and 60% filling capacity) and placed into a stainless-steel autoclave. The autoclave was heated to 250 °C at a rate of 2 °C/min under continuous magnetic stirring. Once the temperature reached 250 °C, the stirring was stopped. Finally, the obtained precipitate was separated from the colloidal solution using centrifugation at 6000 rpm for 10 min, washed several times using ethanol and DI water, and air dried at 80 °C for a day. This reaction was repeated for different synthesis conditions to monitor the growth mechanism.

2.2. Conjugation of chlorin e6 (Ce6) with mesoporous $GdNbO_4:Eu^{3+}$ nanospheroids ($GdNbO_4:Eu^{3+}$@Ce6)

The conjugation of the Ce6 with mesoporous $GdNbO_4:Eu^{3+}$ nanospheroids was carried out using a standard N-(3-dimethylaminopropyl)-N′-ethylcarbodiimide hydrochloride (EDC)/N-hydroxysuccinimide (NHS)-coupling method. A nanocarrier solution was prepared by dispersing 0.5 mM $GdNbO_4:Eu^{3+}$ nanospheroids in 1 ml PBS. The photosensitizer solution was prepared by dissolving 0.3 mg of Ce6 in 1 ml of ethanol, into which equal amounts (40 mg) of EDC and NHC were added in sequence and the carboxyl group of Ce6 was activated by mixing with a rotator at 24 rpm for 15 min. The nanoparticle solution was then added to the Ce6 solution and the $GdNbO_4:Eu^{3+}$@Ce6 mixture was reacted for 24 h. The $GdNbO_4:Eu^{3+}$@Ce6 mixture was subsequently dialyzed against 70% ethanol for 48 h (molecular weight cut-off = 100 kDa).

2.3. Conjugation of folic acid (FA) with $GdNbO_4:Eu^{3+}$@Ce6 ($GdNbO_4:Eu^{3+}$@Ce6@FA)

To produce FA-modified $GdNbO_4:Eu^{3+}$@Ce6 nanospheroids, 1 mM of FA was dissolved in 1 ml of dimethyl sulfoxide solution and activated by mixing it with the 1 mM EDC and 1 mM NHS for 15 min using a rotation at 24 rpm. Following this, 100 µL of $GdNbO_4:Eu^{3+}$@Ce6 solution was added to the activated FA solution and reacted for 24 h to produce $GdNbO_4:Eu^{3+}$@Ce6@FA nanospheroids. The $GdNbO_4:Eu^{3+}$@Ce6@FA nanospheroids were then dialyzed against DI water for 48 h using a 100 kDa dialysis membrane to remove the unreacted FA. After dialysis, $GdNbO_4:Eu^{3+}$@Ce6@FA nanospheroids were lyophilized and used for experimental analysis.

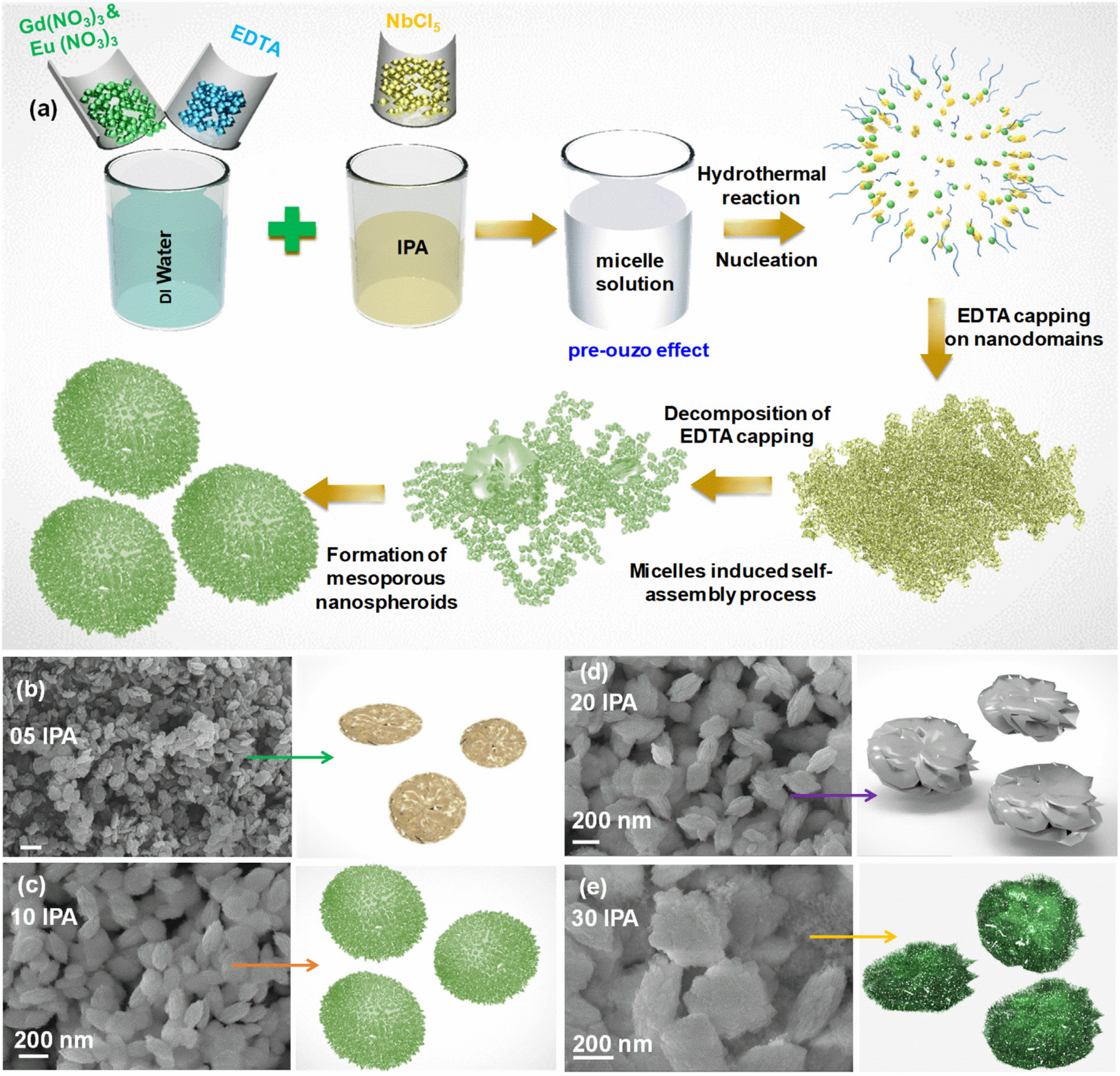

Fig. 1. (a) Schematic for the production of the pre-ouzo effect induced $GdNbO_4$ nanospheroids. The DI water and IPA solvent interface effect (total volume of DI water and IPA = 75 ml) in the formation of $GdNbO_4:Eu^{3+}$ nanostructures; FE-SEM images show the pre-ouzo effect enabled formation of (b) non-mesoporous nanoparticles (c) micelles induced nanodomains self-assembled into nanospheroids, and (d and e) lamellar induced nanoplates self-assembled into layered nanostructures.

3. Results and discussion

3.1. Morphological analysis and growth mechanism

To create the mesoporous $GdNbO_4:Eu^{3+}$ nanostructures, a number of hydrothermal experiments were conducted. The final products were obtained by optimizing different reaction parameters, such as the co-solvent, the concentration of the capping agent, reaction temperature and reaction time, based on controlled experiments. Fig. 1a presents a schematic illustration of the formation of pre-ouzo effect induced mesoporous $GdNbO_4:Eu^{3+}$ nanospheroids. $NbCl_5$, which decomposes when mixed with water but is highly soluble in alcohol, was used as the Nb source. To observe the effect of the solvent interface on the growth of the $GdNbO_4:Eu^{3+}$nanospheroids, experiments were conducted by varying the ratio of isopropanol and de-ionized (DI) water (total volume = 75 ml) at an EDTA concentration of 0.012 g, a reaction temperature of 250 °C and time of 15 h. High-resolution field emission scanning electron microscopy (HR FE-SEM, hereafter referred to simply as FE-SEM) images and corresponding schematic illustrations are displayed in Fig. 1b-e. $NbCl_5$ was dissolved in isopropanol, where it formed niobium isopropoxide, a process which can be described by the following chemical reaction:

$$NbCl_5 + 5(C_3H_7OH) \rightarrow Nb(OC_3H_7)_5 + 5HCl$$

$NbCl_5$ and isopropanol play key roles in the formation of mesoporous nanospheroids. After mixing with the aqueous Gd solution, a ternary system is established and the pre-ouzo effect arises, which allows micelles to form without the use of any surfactant or detergents and assists in the formation of mesoporous $GdNbO_4:Eu^{3+}$ nanostructures under high-temperature hydrothermal conditions. The pre-ouzo effect is an analogy to the ouzo effect, in which the two solvents must be miscible and the solute should be highly soluble in one solvent and poorly soluble in the other [41,42]. Here, either $NbCl_5$ or $Nb(OC_3H_7)_5$ is highly soluble in isopropanol but reacts with DI water and $Gd(NO_3)_3{\cdot}6H_2O$ is soluble in both DI water and isopropanol. Therefore, a milky white emulsion was immediately formed (Fig. 1a) when the Nb

$(OC_3H_7)_5$ solution was mixed with the aqueous Gd solution where the isopropanol assumed not only to act as an interface between the water and $Nb(OC_3H_7)_5$ but also to play a key role as a hydrotrope that mediates the solubility of $Nb(OC_3H_7)_5$.

This emulsion was further treated under hydrothermal conditions for different ratios of DI water and isopropanol. When the ratio of DI water and isopropanol was fixed at 70:5 ml:ml, non-mesoporous $GdNbO_4:Eu^{3+}$ nanoparticles with non-uniform sizes were observed (Fig. 1b), indicating that the reaction was not completed. When the ratio of DI water and isopropanol was set at 65:10, uniform mesoporous nanospheroids formed (Fig. 1c). Under these conditions, $GdNbO_4:Eu^{3+}$ nanodomains are clearly visible on the nanospheroids, indicating that a cooperative assembly process, via the non-directional interaction between micelles and the $GdNbO_4:Eu^{3+}$ nanodomains, is the main driving force in nanospheroid formation. $GdNbO_4:Eu^{3+}$ nanospheroid formation based on micellar mediation was inspired by the Schöttl et al.'s [43] research on surfactant-free micellar aggregates. When the ratio of DI water and isopropanol was changed to 55:20, 45:30, 35:40, and 25:50, the pores of the nanospheroids disappeared and the size of the particles increased and formed like self-assembled nanoplate layered nanostructures (Fig. 1d-e and Fig. S1a-b). This change in the nanostructure might be due to an increase in the size of micelles, leading to the formation of a lamellar phase. These results are in agreement with the Liu et al.'s [44] report on the formation of mesoporous silica particles, and Song et al.'s [45] research on the viscosities of binary and ternary water-alcohol mixtures. When the ratio of water and isopropanol was increased to 15:60, $GdNbO_4:Eu^{3+}$ microparticles were observed (Fig. S1c), which were formed due to the aggregation of layered $GdNbO_4:Eu^{3+}$nanostructures.

The concentration of the complexing agent EDTA plays a key role in the growth of mesoporous nanospheroids; therefore, the formation of $GdNbO_4:Eu^{3+}$ nanospheroids was also studied as a function of the EDTA concentration, with all other parameters kept constant (a DI water and isopropanol ratio of 65:10 ml:ml, a reaction temperature of 250 °C, and a reaction time of 15 h), as shown in Fig. S1d-g. The effect of EDTA concentration is summerized in Section I of the Supporting Information. At the optimal EDTA concentration (0.012 g), the $GdNbO_4:Eu^{3+}$ nanodomains (~5 nm in size) self-assembled into nanospheroid-like nanoparticles (~180 nm in size) with a mesoporous structure (Fig. 1c and Fig. S1e). The mesoporous nanospheroids were almost uniform in size and shape. Under these conditions, EDTA balanced the growth rate by restricting the development of branches in different directions. The results suggests that at a particular condition, it is possible to obtain mesoporous $GdNbO_4:Eu^{3+}$ nanoparticles due to the pre-ouzo effect.

The reaction temperature and reaction time are also key parameters in the formation of $GdNbO_4:Eu^{3+}$ nanospheroids, so the effect of these two variables was also studied under hydrothermal conditions. First, experiments were carried with varying reaction temperatures and all other parameters kept constant (EDTA = 0.012 g, reaction time = 15 h DI water to isopropanol ratio = 65:10 ml:ml), as shown in Fig. 2 and Fig. S2**.** When the reaction temperature was 200 °C, no specific morphology was observed but nanodomains containing irregular blocks appeared (Fig. 2a), which might be due to the simultaneous chelation and over-capping effect of EDTA. This EDTA capping restricts the increase in $GdNbO_4:Eu^{3+}$ particle size, which favors the formation of nanodomains-assembled nanospheroids at elevated reaction temperatures. When the reaction temperature was increased to 220 °C, $GdNbO_4:Eu^{3+}$ nanodomains (Fig. 2b) were observed with a crystalline monoclinic phase because EDTA capping begins to decompose at 220 °C, facilitating the self-assembly of $GdNbO_4:Eu^{3+}$ nanodomains via micellar mediation. When the reaction temperature was further increased to 240 °C, uniform nanospheroid-like mesoporous nanoparticles (Fig. 2c and Fig. S2a) with well-defined monoclinic $GdNbO_4:Eu^{3+}$ diffraction peaks (Fig. S3a) were observed, where the EDTA capping effect weakening gradually and the micelles actively playing a key role in the formation of a mesoporous structure. At 250 °C, well-defined mesoporous $GdNbO_4:Eu^{3+}$ nanospheroids were formed (Fig. 2d, and Fig. S2b), along with the appearance of all $GdNbO_4:Eu^{3+}$ X-ray diffraction (XRD) peaks (Fig. S3a), indicating the presence of optimal EDTA and micellar effects. However, at 260 °C, the porous nature of the $GdNbO_4:Eu^{3+}$ nanospheroids disappeared, and lamellar-induced nanospheroids with enhanced crystallinity were obtained at 280 °C, as shown in Fig. 2e and f, and Fig. S2c and d. The enhanced crystallinity and disappearance of the mesoporous nature might be due to the enhanced effect of Ostwald's ripening process at elevated reaction temperature. From the XRD patterns (Fig. S3a), the intensity ratio of the diffraction peaks at 28.32°/29.79° clearly varies with increasing temperature, indicating that preferential orientation was strongly dependent on the reaction temperature.

HR-TEM image revealed lattice fringes and empty spaces (highlighted with circles in Fig. 2g), illustrating the mesoporous nature of the $GdNbO_4:Eu^{3+}$ nanospheroids. Lattice fringes were observed across the entire nanodomains regions with a uniform spacing of 2.68 Å, indicating the successful formation of $GdNbO_4:Eu^{3+}$ composite nanodomains. Fig. 2h presents the SAED pattern, which exhibited bright spots on the ring pattern, and the d-spacing values were in agreement with those for the monoclinic phase of $GdNbO_4:Eu^{3+}$. These results also support the formation of mesoporous nanospheroids with $GdNbO_4:Eu^{3+}$ nanodomains. To identify the elements present in the $GdNbO_4:Eu^{3+}$ nanospheroids, energy dispersive X-ray spectroscopy (EDS) was carried out. Fig. 2i shows the EDS spectrum (magnified image presented in Fig. S2e) for the $GdNbO_3:Eu^{3+}$ nanospheroids, indicating the presence of Gd, Nd, Eu, C, and O ions and confirming that the Nb ions had occupied L shells, Gd and Eu had occupied both L and M shells, and C and O ions had occupied K-shells. Fig. 2j presents the corresponding color mapping of the elements present in the $GdNbO_4:Eu^{3+}$ nanospheroids.

The effect of reaction time is presented in the Supporting Information (Fig. S4, Section II in Supporting Information), illustrating the capping effect of EDTA and simultaneous self-assembly of $GdNbO_4:Eu^{3+}$ nanodomains in the formation of mesoporous $GdNbO_4:Eu^{3+}$ nanospheroids over the course of the reaction time. Mesoporous $GdNbO_4$ or $GdNbO_4:Eu^{3+}$ nanospheroids with an average particle size of 180 nm were observed to form under the following growth conditions (a solvent ratio of 65 ml of DI water to 10 ml of isopropanol, 0.012 g of EDTA, a reaction temperature of 250 °C, and a reaction time of 15 h). Based on the morphological results, we posit that the formation mechanism of $GdNbO_4:Eu^{3+}$ nanospheroids is micelle formation and nucleation induced by the pre-ouzo effect, the simultaneous complexation and capping of the nanodomains, the decomposition of EDTA capping, the availability of nanodomains for self-assembly and finally, the self-assembly of nanodomains with micellar mediation to form $GdNbO_4:Eu^{3+}$ nanospheroids. A schematic diagram of the growth mechanism is presented in Fig. 1a. Due to their similar ionic radii and the same oxidation states, pure $GdNbO_4$ and $GdNbO_4:Eu^{3+}$ exhibited similar morphologies.

3.2. *Structural properties*

To examine the structural properties of the synthesized mesoporous $GdNbO_4$ nanospheroids, Fourier transform infrared (FTIR), Raman and X-ray photoelectron spectroscopy (XPS) investigations were conducted. Fig. 3a presents the transmittance mode FTIR spectrum for the mesoporous $GdNbO_4:Eu^{3+}$ nanospheroids. The FTIR spectrum exhibited vibrational frequencies with band maxima at 3574, 3190, 1580, 1400, 1094, 817, and 652 cm^{-1}. A broadband appeared between 2500 and 3800 with band maxima at 3574 and 3190 cm^{-1}, which are associated with H-bonded –OH symmetric stretching vibrations. Nihonyanagi et al. [46] reported that the splitting of –OH vibrations is due to intermolecular or intramolecular couplings. This is also applicable to the $GdNbO_4$ nanospheroids because micelles were formed due to the pre-

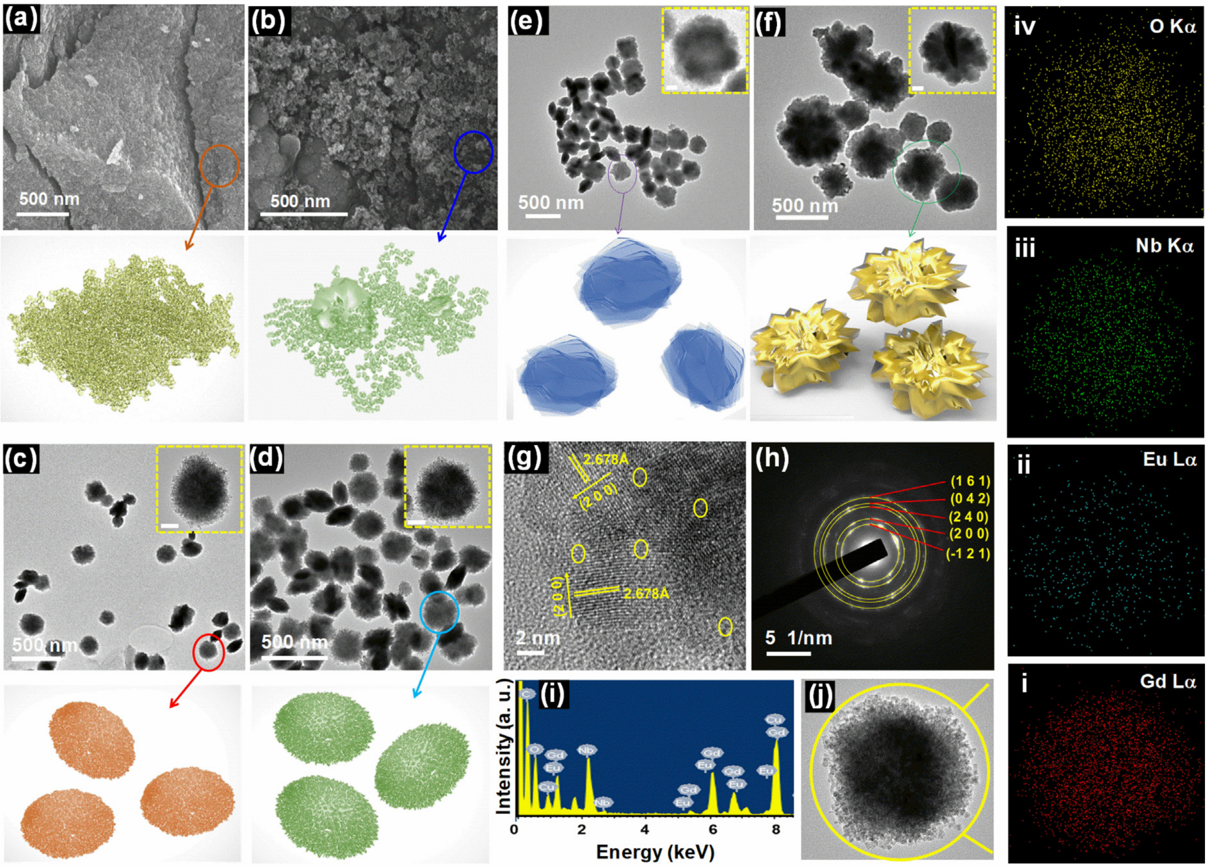

Fig. 2. FE-SEM and TEM images and corresponding schematics showing the effect of reaction temperature on the formation of $GdNbO_4$ nanospheroids (a) 200 °C, (b) 220 °C, (c) 240 °C, (d) 250 °C, (e) 260 °C and (f) 280 °C (inset scale bar = 50 nm). (g) HR-TEM image, (h) SAED pattern and (i & j) EDS and corresponding color mappings of Gd, Eu, Nb, and O.

ouzo effect in the interaction between water and niobiumisopropoxide/isopropanol, where intermolecular couplings formed. The peak with a maximum frequency at 1580 cm^{-1} is attributed to the −COO coordinated asymmetric stretching vibrational band, which indicates EDTA chelation between Gd and Nb ions. The peaks with maxima at 1400 and 1094 cm^{-1} are related to the symmetric stretching vibrations of −COO and −CO, respectively. The broad band between 500 and 900 cm^{-1} exhibited two band maxima at 817 and 652 cm^{-1}, which are related to the O−Nb−O bridge and Nb−O stretching vibrations, respectively. To verify the effect of EDTA, the FTIR spectra were measured as a function of reaction temperature (Fig. S3b). The decrease in the vibrational band intensities between 1000 and 1800 cm^{-1} with increasing reaction temperature confirmed the decomposition of EDTA.

Fig. 3b shows the Raman spectrum of the mesoporous $GdNbO_4:Eu^{3+}$ nanospheroids. The spectrum exhibits Raman-active modes at 106, 170, 232, 332, 417, 453, 638, 691 and 800 cm^{-1}. When compared to earlier reports [30,31], the peaks were all broader and some peaks (106, 170 and 800 cm^{-1}) were red-shifted, indicating the presence of nanodomains within the nanospheroids. Due to the effect of these nanodomains, the theoretically predicted 18 Raman-active modes were not well differentiated. However, the symmetric (ν_1 and ν_2) and antisymmetric (ν_3 and ν_4) vibrational modes of fergusonite-structured monoclinic $GdNbO_4:Eu^{3+}$ were observed in the Raman spectrum. The Raman bands appearing at 800 and 332 cm^{-1} belong to the ν_1 and ν_2 modes, respectively, of the Nb−O vibrational in the NbO_4 tetrahedral structure. The ν_3 and ν_4 vibrational modes of Nb−O appeared at 638 and 417 cm^{-1}, respectively.

The chemical composition and oxidation states of the mesoporous $GdNbO_4:Eu^{3+}$ nanospheroids were further observed using XPS analysis. The XPS survey of $GdNbO_4:Eu^{3+}$ (Fig. S5), indicating the presence of Gd, Eu, Nb, O and C. Fig. 3c shows the high-resolution Gd 4d spectrum, and peaks at binding energies of 140.5, 143.1, and 147.7 eV, which were assigned to Gd/Eu 4d, Gd $4d_{5/2,}$ and Gd $4d_{3/2,}$ respectively, within the $GdNbO_4:Eu^{3+}$ compound. The inset of Fig. 3c presents the high-resolution Eu 3d spectrum with the peak closely fitting a binding energy of 1134.5 eV, which can be ascribed to Eu $3d_{5/2}$. The appearance of Eu 4d and Eu $3d_{5/2}$ confirmed the doping of Eu^{3+} ions at Gd^{3+} sites. Similarly, Nb ions in $GdNbO_4:Eu^{3+}$ exhibited an Nb 3d spectrum of Nb $3d_{5/2,}$ Nb $3d_{5/2,}$ and Nb $3d_{3/2}$ at 206.4, 207.2, and 209.3 eV, respectively, with Nb^{5+} and Nb^{4+} oxidations states (Fig. 3d). Fig. 3e presents the high-resolution O 1s spectrum, which was de-convolved into several peaks at binding energies of 529.1, 529.6, 530.2, 531.3, 532.1, and 532.6 eV. These results further confirmed the successful formation of $GdNbO_4:Eu^{3+}$.

The specific surface area and pore size distribution of the $GdNbO_4:Eu^{3+}$ nanospheroids were observed by measuring the corresponding Brunauer–Emmett–Teller (BET) and Barrett–Joyner–Halenda (BJH) curves (Fig. 3f). N_2 adsorption and desorption curves confirmed a type IV isotherm with an H4 hysteresis loop, supporting the mesoporous nature of the particles [47]. The specific surface area (from BET analysis) and the average pore diameter (using the BJH method) of the $GdNbO_4:Eu^{3+}$ nanospheroids were found to be around 34.4 m^2/g and 9.3 nm, respectively.

3.3. Photoluminescence properties

Fig. 4a and c show the photoluminescence (PL) excitation and emission spectra of $GdNbO_4$ nanospheroids, respectively. The PL excitation and emission spectra exhibited broadband excitation and emission between the regions of 200–500 nm and 400–650 nm,

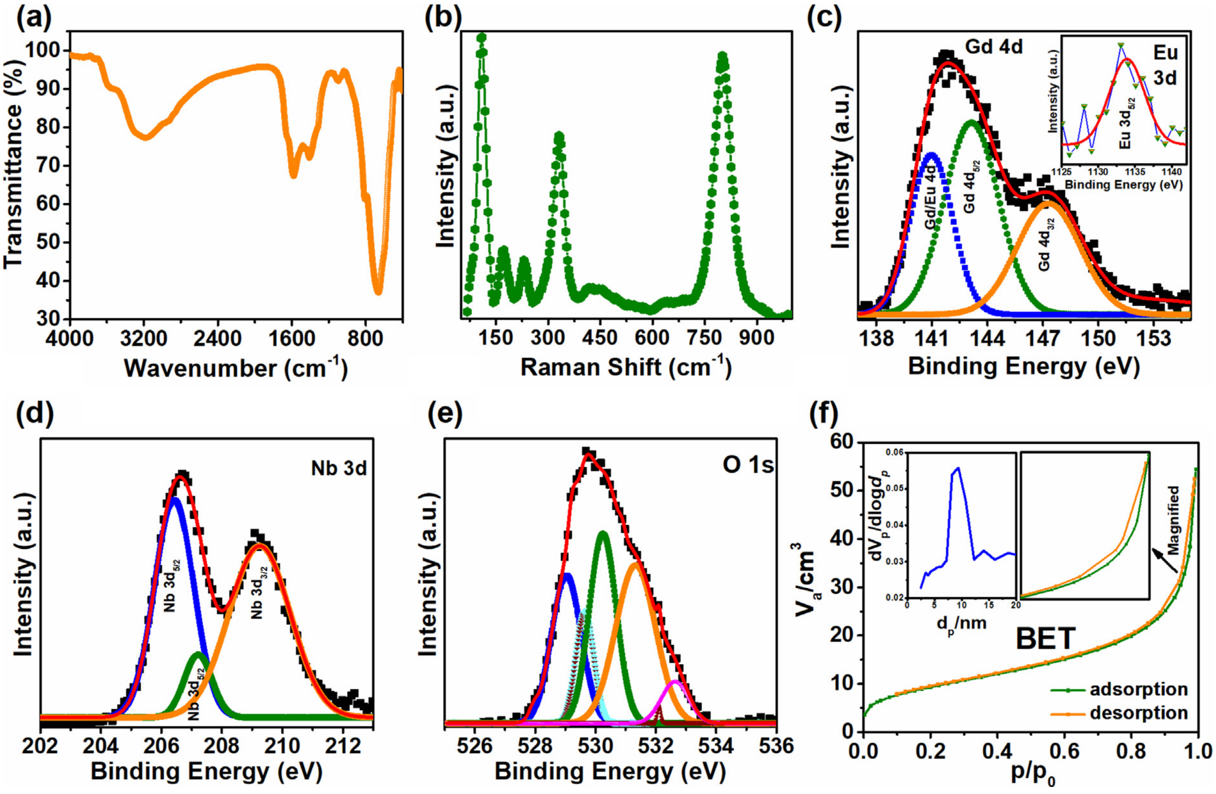

Fig. 3. Structural properties of $GdNbO_4:Eu^{3+}$ nanospheroids: (a) FTIR, (b) Raman, (c–e) high magnification XPS spectra for Gd (inset Eu), Nb and O, respectively, and (f) BET.

respectively. For clarity, the PL excitation spectrum was de-convolved using Gaussian fitting, leading to two intense bands with band maxima at 346 and 410 nm and one weak band with a band maximum at 294 nm (Fig. 4a). The excitation band with a band maximum at 294 nm was due to the typical $O^{2-} \rightarrow Nb^{5+}$ ligand to metal charge transfer transition (LMCT), which is similar to earlier reports, in which LMCT band was observed between 200 and 300 nm [29,30,48,49]. Liu et al. [29] reported a comparison of LMCT intensities between bulk and nanocrystalline $GdNbO_4$ host lattices and concluded that LMCT intensity depends on the crystallinity, the size of the particles, and the number of surface defects. All of these studies reported an excitation spectrum between 200 and 310 nm but not in the NUV (315–400 nm) and visible regions. In contrast, the $GdNbO_4$ nanospheroids in the present study exhibited intense broadband excitations in the NUV and visible regions. The PL excitation spectra as a function of emission wavelength are presented in Fig. S6a and b, and exhibited similar excitation bands except their intensities. According to Blasse et al. [50], the angle between Nb—O—Nb plays a key role in deciding the position of excitation bands. If the angle of Nb—O—Nb increases (Fig. 4b), the excitation band maximum appears at a lower energy level due to the strong delocalization of electronic wavefunctions, which results in the broadening of energy bands. Fulle et al. [51] reported that fergusonite-type $RENbO_4$ exhibits a three-dimensional framework with irregular NbO_6 and REO_8 units. In both units the Nb and RE ions occupy 4e Wycoff positions with two-fold symmetry. Nb ions in the 4e Wycoff position bond with six oxygen atoms with four shorter and two longer bond lengths. The two longer bonds in NbO_6 octahedra show significant variation with a change in the RE ion, meaning that the bond lengths of Nb—O depend on the ionic radius and position of the RE ions. The observation that the variation in bond length influences the bond angle of Nb—O—Nb can also be applied to nanoparticles. In the $GdNbO_4$ nanospheroids, the nanospheroid was developed via the self-assembly of $GdNbO_4$ nanodomains, in which the local distortion between the NbO_6 octahedrons might occur, resulting in an increase in the Nb—O—Nb bond angle. To examine this, the unit cell parameters were calculated for the XRD patterns of $GdNbO_4$ nanospheroids, and the obtained lattice constants were a = 5.409 Å, b = 11.088 Å, c = 4.605 Å, β = 87.677°, and V = 276.215 Å^3. The lattice parameters from the reference JCPDS card (#022-1104) are a = 5.369 Å, b = 11.090 Å, c = 5.105 Å, β = 94.550°, and V = 303.010 Å^3. It is thus clear that the unit cell volume of the $GdNbO_4$ nanospheroids decreases due to the decrease in the lattice constant c, indicating that lattice distortion occurred in the c-direction. The decrease in length in the c-direction is greater when compared to the increase in length in the a-, and b- directions, resulting in a greater bond angle in Nb—O—Nb.

The PL emissions of the $GdNbO_4$ nanospheroids (Fig. 4c) also exhibited different properties compared to previously reported $GdNbO_4$ emission spectra, where broadband emissions were observed in the visible region between 400 and 600 nm with a band maximum at around 440 nm. For the $GdNbO_4$ nanospheroids, the broadband emissions had band maxima at 440, 483 and 522 nm. The appearance of additional peaks at 483 and 522 nm is due to the $GdNbO_4$ nanodomains. Similar emission properties were reproduced even with different excitation wavelengths (Fig. S6c).

The PL excitation and emission of $GdNbO_4:Eu^{3+}$ is presented in Fig. 4d and e. Fig. 4d shows the excitation spectrum of $GdNbO_4:Eu^{3+}$, which exhibited a broadband with a band maximum at 273 nm along with f-f transitions at 361 nm ($^7F_0 \rightarrow {}^5D_4$), 381 nm ($^7F_0 \rightarrow {}^5G_2$), 394 nm ($^7F_0 \rightarrow {}^5L_6$), 415 nm ($^7F_0 \rightarrow {}^5D_3$) and 464 nm ($^7F_0 \rightarrow {}^5D_2$). The deconvolved PL excitation spectra clearly displayed broad bands with band maxima at 257, 294 and 366 nm. The excitation band with a band maximum at 257 nm was due to the charge transfer from the completely filled 2p orbitals of O^{2-} ions to the partially filled 4f orbitals of Eu^{3+} ions, which is also known as the charge transfer band (CTB). The other two broad bands related to the LMCT and the presence of nanodomains in the $GdNbO_4:Eu^{3+}$ nanospheroids. Interestingly, the intensity of the LMCT in the $GdNbO_4:Eu^{3+}$ nanospheroids increased compared to the host $GdNbO_4$, which might be due to the overlap of the

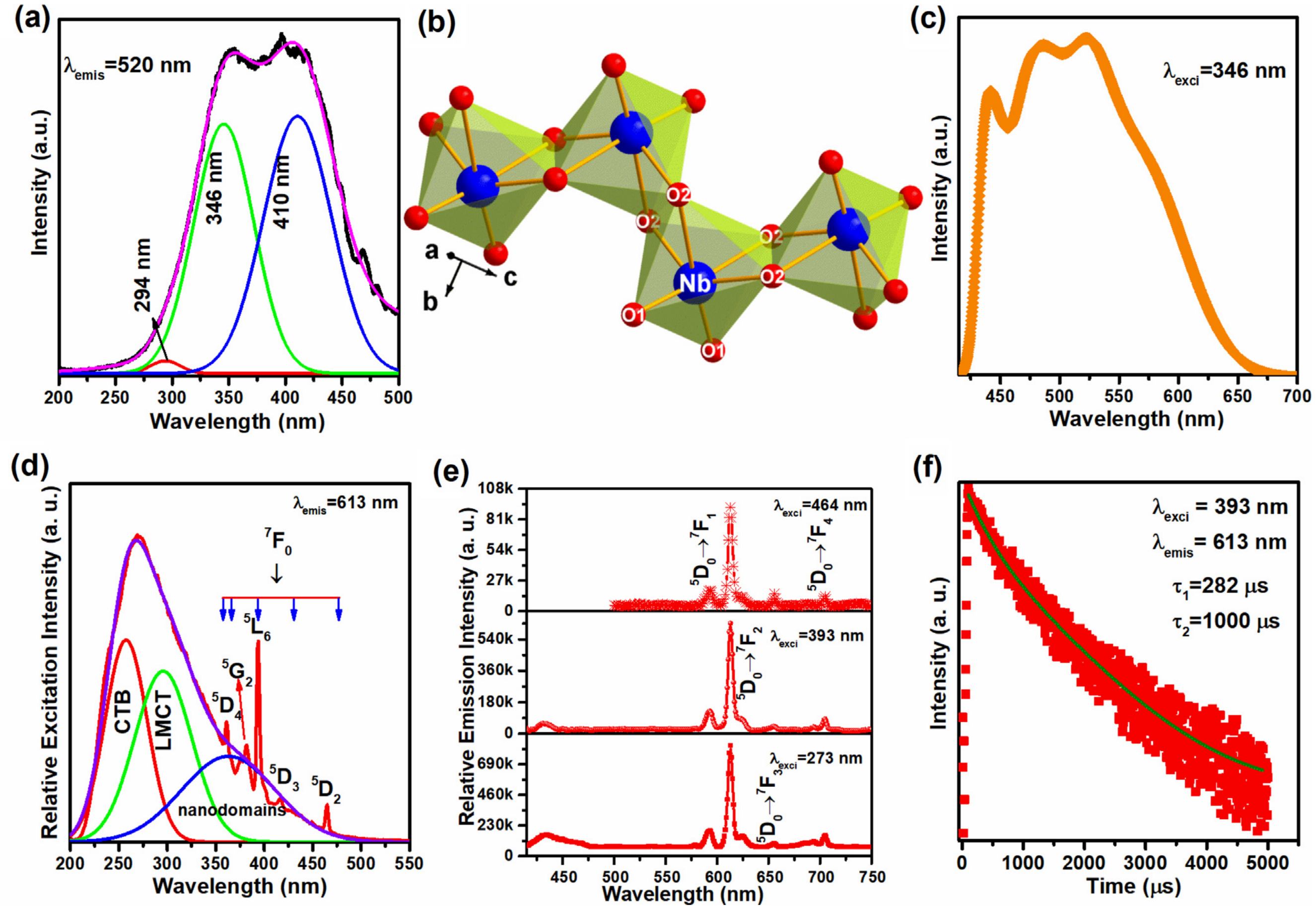

Fig. 4. Photoluminescence properties of mesoporous $GdNbO_4$ and $GdNbO_4:Eu^{3+}$ nanospheroids. (a) Excitation spectrum, (b) Nb-O octahedral crystal structure and (c) emission spectrum of $GdNbO_4$ nanospheroids. (d) Excitation and (e) emission spectra of $GdNbO_4:Eu^{3+}$ nanospheroids along with (f) the decay curve.

CTB and LMCT. In addition, the band maximum shifted from 346 to 366 nm, which may be due to the merging of the 346 and 410 nm excitation bands. The increase in LMCT intensity and the merging of the two bands were assumed to facilitate the efficient energy transfer from the CTB to the lower energy levels, such as the f-f transitions, of the Eu^{3+} ions via the LMCT and merged nanodomain band. In the literature, nanocrystalline or bulk $GdNbO_4:Eu^{3+}$ phosphors have been reported to exhibit an intense CTB between 200 and 300 nm and very poor f-f transitions in the NUV region [29,30,52]. Therefore, the excellent excitation properties in the NUV and visible regions, which are useful for biomedical applications, are advantageous features of the $GdNbO_4:Eu^{3+}$ nanospheroids in this study. The intense excitation bands exhibited by $GdNbO_4:Eu^{3+}$ in the UV, NUV, and visible regions raise the possibility of multifunctional applications, such as solid-state lighting, photocatalytic, and biomedical applications. In particular, NUV and visible excitations are suitable for biomedical applications.

Fig. 4e shows the PL emission spectra of the $GdNbO_4:Eu^{3+}$ nanospheroids as a function of excitation wavelength. At different excitations, the spectra exhibited similar emission bands in the red region (except for their intensity) due to intra-configurational f-f transitions of $^5D_0 \rightarrow {}^7F_1$, $^5D_0 \rightarrow {}^7F_2$, $^5D_0 \rightarrow {}^7F_3$, and $^5D_0 \rightarrow {}^7F_4$ at 592, 613, 655 and 705 nm, respectively. In addition, for 273 and 393 nm excitations, the spectra exhibited a weak broadband emission with a band maximum at 440 nm, which is related to the $NbO_4{}^{3-}$ group, but nanodomain emissions were completely suppressed with a doping of 5 mol% Eu^{3+} ions in the $GdNbO_4$ host lattice (Fig. S6d), indicating efficient energy transfer from the $GdNbO_4$ nanodomain host to Eu^{3+} ions. Of the f-f transitions appearing in the emission spectra of the $GdNbO_4:Eu^{3+}$ nanospheroids, the hypersensitive transition $^5D_0 \rightarrow {}^7F_2$ displayed more intense emissions than did other transitions. In particular, the asymmetry ratio of the hypersensitive to magnetic dipole ($^5D_0 \rightarrow {}^7F_2/{}^5D_0 \rightarrow {}^7F_1$) transitions indicates the lack of inversion symmetry of Eu^{3+} ions in the $GdNbO_4$ nanospheroids and confirmed the presence of an REO_8 unit with two-fold rotational symmetry similar to a NbO_6 unit occupying the 4e crystallographic site [51].

The decay curve of $GdNbO_4:Eu^{3+}$, which was measured via excitation 393 nm and monitoring the emission wavelength at 613 nm, is presented in Fig. 4f. The decay curve closely fit the bi-exponential [$I(t) = I_0 + A_1 exp(-t/\tau_1) + A_2 exp(-t/\tau_2)$] function, where I_0 and I denote the luminescence intensity at time zero and *t*, respectively, τ_1 and τ_2 are the short and long lifetimes, respectively, and A_1 and A_2 are the constants. The calculated τ_1 and τ_2 values were 282 and 1000 µs, respectively. Liu et al. [29] reported that the decay curve of $GdNbO_4:Eu^{3+}$ phosphor closely fit a single exponential function when measured under an excitation of 261 nm, and Yang et al. [30] also reported a single exponential function for $GdNbO_4:Eu^{3+}$ under a 306 nm excitation. Both reports are based on nanocrystalline phosphors. For the $GdNbO_4:Eu^{3+}$ nanospheroids, in the present study, the decay curve fit a bi-exponential function well, indicating efficient energy transfer from the NbO_6 octahedral units to the Eu^{3+} ions. Based on the PL properties, we suggest that the pre-ouzo effect induced self-assembly of nanodomains into $GdNbO_4:Eu^{3+}$ nanospheroids facilitates the energy transfer between the NbO_6 octahedral units and Eu^{3+} ions. The present study represent the first to report on $GdNbO_4$ and $GdNbO_4$ sensitized luminescence properties.

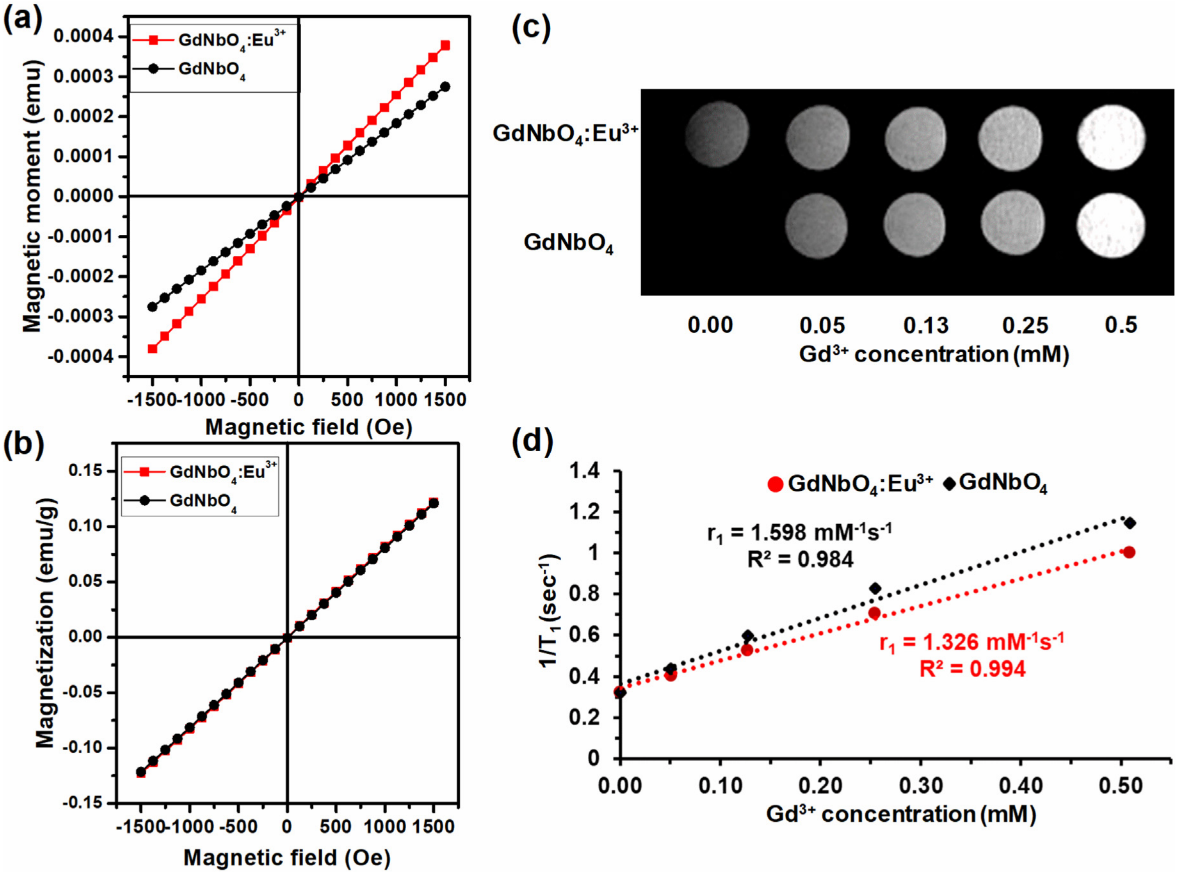

Fig. 5. Magnetic-field-dependent variation in the (a) magnetic moment and (b) magnetization of mesoporous $GdNbO_4$ and $GdNbO_4:Eu^{3+}$ nanospheroids. (c) T1-weighted MRI images and (d) longitudinal relaxation times of mesoporous $GdNbO_4$ and $GdNbO_4:Eu^{3+}$ nanospheroids at different Gd^{3+} ion concentrations.

3.4. Magnetic properties

To understand the magnetic behavior, such as magnetization and susceptibility, of the $GdNbO_4$ and $GdNbO_4:Eu^{3+}$ nanospheroids, room temperature super-conducting quantum interface device (SQUID) analysis was conducted as a function of the applied magnetic field. Magnetization was obtained by measuring the magnetic moment per unit mass. Fig. 5a and b shows the variation in the magnetic moment and magnetization of the $GdNbO_4$ and $GdNbO_4:Eu^{3+}$ nanospheroids as a function of the applied magnetic field. The $GdNbO_4$ nanospheroids with and without Eu^{3+} ions exhibited paramagnetic behavior with zero coercivity and remanent magnetization suggesting the absence of hysteresis. Magnetization was linearly dependent on the magnetic field, which indicated that there was a single paramagnetic phase at room temperature (Fig. 5b). There was no significant difference observed in the magnetization of $GdNbO_4$ and $GdNbO_4:Eu^{3+}$ nanospheroids due to the absence of ferromagnetic impurities in both samples. The magnetic behavior of both samples mainly originated from unpaired f–electrons of lanthanide ions. In addition, the susceptibilities of $GdNbO_4$ and $GdNbO_4:Eu^{3+}$ nanospheroids, which were evaluated from magnetization vs. applied magnetic field data, were 8.09×10^{-5} emu g^{-1} Oe^{-1} and 8.21×10^{-5} emu g^{-1} Oe^{-1}, respectively. The paramagnetic behavior of the $GdNbO_4$ and $GdNbO_4:Eu^{3+}$ nanospheroids indicates their feasibility for use in MRI imaging for medical diagnosis.

3.5. Multimodal bioimaging and photodynamic therapy

Hydrodynamic particle size and zeta potential are influential factors for successful biomedical applications. Dynamic Light Scattering (DLS) analysis was conducted without surface modification of GdNbO4:Eu^{3+} nanospheroids and the results are presented in Fig. S7a-d (Section III, Supporting Information). Hydrodynamic size and zeta potential of $GdNbO_4:Eu^{3+}$ nanospheroids were confirmed to be of a uniform shape with favorable dispersion and stability in DI water and Dulbecco's Modified Eagle Medium (DMEM) cell culture media. To examine the feasibility of $GdNbO_4:Eu^{3+}$ nanospheroids for use in biomedical applications, dual-modal imaging involving MRI and optical imaging was conducted. Because of the availability of Gd^{3+} ions in the mesoporous $GdNbO_4$ and $GdNbO_4:Eu^{3+}$ nanospheroids, the synthesized mesoporous particles act as T1 MRI contrast agents. To assess the MRI performance of mesoporous $GdNbO_4$ and $GdNbO_4:Eu^{3+}$ nanospheroids, the MRI signals from the solution were examined as a function of Gd^{3+} ion concentration, and the resulting images are presented in Fig. 5c. The longitudinal (1/T1) relaxation time of the mesoporous $GdNbO_4$ and $GdNbO_4:Eu^{3+}$ nanospheroids was plotted against Gd^{3+} ion concentration (Fig. 5d). The MRI T1 weighted signals increased linearly with an increasing concentration of Gd^{3+} ions. The specific relaxivity (r_1) was calculated based on the relationship between longitudinal relaxation time and Gd concentration (from 0.05 to 0.5 mM, Fig. 5d); r_1 was found to be 1.598 mM^{-1} s^{-1} and 1.326 mM^{-1} s^{-1} for the mesoporous $GdNbO_4$ and $GdNbO_4:Eu^{3+}$ nanospheroids, respectively. The higher r_1 of $GdNbO_4$ compared to the $GdNbO_4:Eu^{3+}$ nanospheroids might be due to the efficient exchange of Gd^{3+} ions with the surrounding water protons [53]. The obtained r_1 values were similar or better than those reported for $NaGdF_4:Er^{3+}$, $Yb^{3+}/NaGdF_4$, CaF_2:Gd,Er,Yb and CaF_2:Gd,Er,Tm nanoparticles [54,55].

HCT116 and SW680 cell lines were used to examine the optical imaging capability of the $GdNbO_4:Eu^{3+}$ nanospheroids. The penetration capability of the $GdNbO_4:Eu^{3+}$ nanospheroids with HCT116 and SW680 cells was examined using fluorescence-assisted cell sorting (FACS) analysis, which is a specialized form of flow cytometry. Fig. 6a and b presents FACS histograms for the HCT116 and SW680 cell lines

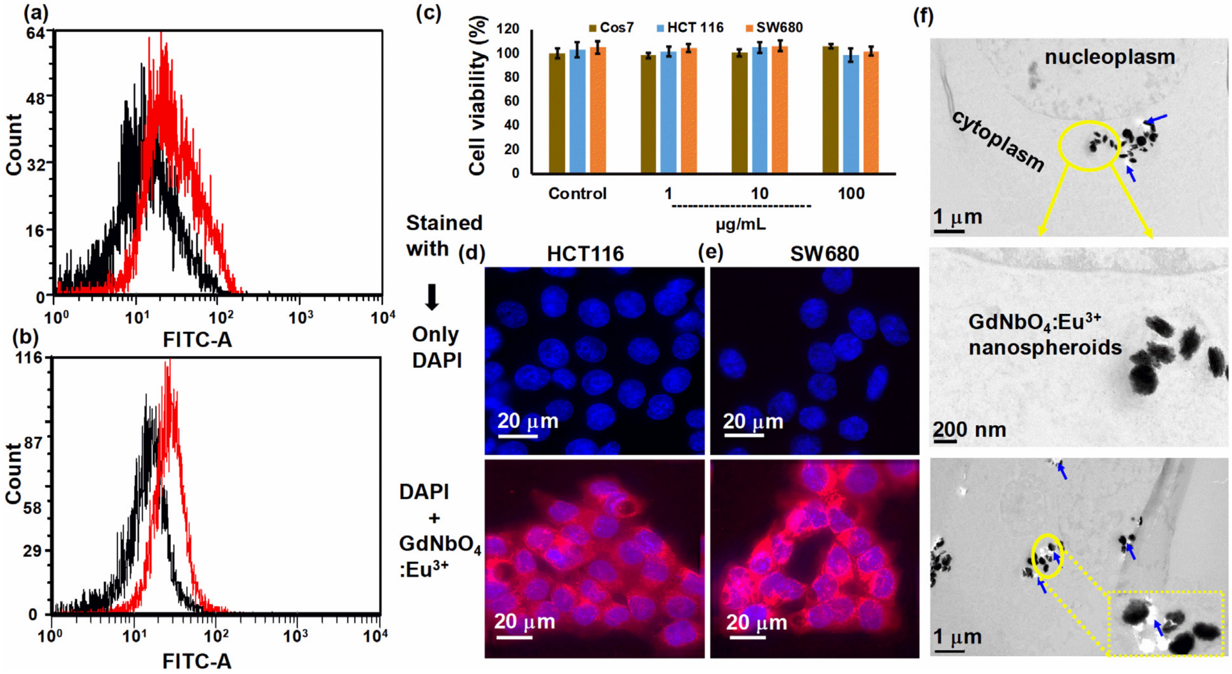

Fig. 6. FACS histograms of control and $GdNbO_4:Eu^{3+}$ nanospheroid-stained (a) HCT116 and (b) SW680 cells, which exhibited good cellular internalization, (c) XTT assays confirmed the non-toxic nature of the nanospheroids. Confocal microscope images of (d) HCT116 and (e) SW680, which exhibited high resolution red emissions from the cellular cytoplasm and nucleoplasm (scale bar = 20 μm). (f) Bio-TEM images of HCT116 cells after incubation with $GdNbO_4:Eu^{3+}$ nanospheroids (the blue arrows indicate the vesicles).

with and without $GdNbO_4:Eu^{3+}$ nanospheroids staining, respectively. It can be observed that the histogram for the $GdNbO_4:Eu^{3+}$ nanospheroid stained HCT116 and SW680 cells had more highly intense FITC regions as compared to the control, indicating good penetration capability. Further, XTT assays were used to investigate the cytotoxicity of $GdNbO_4$ and $GdNbO_4:Eu^{3+}$ nanospheroids stained COS7, HCT116 and SW680 cells. Fig. S8 and Fig. 6c presents the XTT assay results, which shows that the viabilities of non-cancerous COS7 and cancerous HCT116 and SW680 cells were good for the tested $GdNbO_4$ and $GdNbO4:Eu^{3+}$ nanospheroid concentration range of up to 100 μg/ml, indicating that $GdNbO_4$ and $GdNbO_4:Eu^{3+}$ nanospheroids are suitably biocompatible.

To further confirm the localization of the $GdNbO_4:Eu^{3+}$ nanospheroids within the HCT116 and SW680 cells, in vitro fluorescence microscopy analysis was performed. Fig. 6d and e presents DAPI-alone and $GdNbO_4:Eu^{3+}$ nanospheroid/DAPI merged confocal microscope images confirming that the $GdNbO_4:Eu^{3+}$ nanospheroids emitted a significantly brighter red color from both the cytoplasm and nucleoplasm of the cells. The red emissions from the cytoplasm and nucleoplasm indicates the effective potential uptake of $GdNbO_4:Eu^{3+}$ nanospheroids by cancer cells. To understand the reasons for the cell localization of the nanospheroids, the $GdNbO_4:Eu^{3+}$ nanospheroids were calcined at 300 and 400 °C for 5 h. With increasing calcination temperature of $GdNbO_4:Eu^{3+}$ nanospheroids, the confocal microscope images (Fig. S9a and b) displayed weaker red emissions from calcined $GdNbO_4:Eu^{3+}$ nanospheroid stained cells and almost no emission using 400 °C calcined samples, indicating that the localization of calcined $GdNbO_4:Eu^{3+}$ nanospheroids in the cancer cells decreased as the calcination temperature increased. The same phenomenon was observed in FACS analyses of both HCT116 and SW680 cell lines, where the shift of calcined $GdNbO_4:Eu^{3+}$ nanospheroids stained samples decreased when increasing calcination temperature and no shift was observed for the stained cells with the 400 °C calcined sample (Fig. S9c and d, Supporting Information). The FACS histograms and confocal microscope images display the same results, indicating that the hydrophilic nature of the $GdNbO_4:Eu^{3+}$ nanospheroids gradually changes to a hydrophobic nature. This hydrophobic behavior was due to the loss of the −OH, −CO, and −COO surface functional groups of $GdNbO_4:Eu^{3+}$ nanospheroids with increasing the calcination temperature.

In addition to the above observations, the uptake of $GdNbO_4:Eu^{3+}$ nanospheroids by cancer cells was further confirmed by bio-TEM analysis (Fig. 6f). After incubation with $GdNbO_4:Eu^{3+}$ nanospheroids, vesicles formed in the cytoplasm. The nanospheroids were found in both the vesicles and the cytosol in the cytoplasm and the morphology of the nanospheroids did not change, indicating that the nanospheroids were phagocytized by the HCT116 cells via endocytosis. These results are in good agreement with the FACS and confocal imaging analyses.

We further explored the antitumor activity of $GdNbO_4:Eu^{3+}$@Ce6@FA in PDT. The conjugation of Ce6 and FA with $GdNbO_4:Eu^{3+}$ nanospheroids was carried out via an EDC-NHS-activated condensation reaction and confirmed using TEM and FTIR analyses. TEM images clearly showed the conjugation of Ce6 (Fig. 7a) and both Ce6 and FA with the $GdNbO_4:Eu^{3+}$ nanospheroids (Fig. 7b). A schematic illustration of the conjugations process is presented in Fig. 7c. Compared to the $GdNbO_4:Eu^{3+}$ nanospheroids, the FTIR spectra (Fig. 7d) of $GdNbO_4:Eu^{3+}$@Ce6 and $GdNbO_4:Eu^{3+}$@Ce6@FA exhibited additional vibration modes for N−H, COOH, and C═O at 1495, 1613, and 1652 cm^{-1}, respectively, indicating the successful conjugation of Ce6 and FA with the $GdNbO_4:Eu^{3+}$ nanospheroids. COS7 and HCT116 cells were treated with different doses of $GdNbO_4:Eu^{3+}$@Ce6@FA nanospheroids and incubated for 24 h. PDT was conducted via irradiating with and without 671 nm wavelength laser light for 10 min. After irradiating with light, the cells were incubated for 24 h and XTT assays were conducted. Without laser irradiation, $GdNbO_4:Eu^{3+}$@Ce6@FA nanospheroids did not show any effect on the non-cancerous COS7 cells, whereas, after laser irradiation the survival rate was about 87% when treated with 100 μg/ml (Fig. S10), indicating that no obvious toxicity to the normal cells. As shown in Fig. 7e, without irradiation, cell viability was about 86% when treated with 100 μg/ml of $GdNbO_4:Eu^{3+}$@Ce6@FA nanospheroids, while after irradiation with 671 nm light, the cell survival rate was about 5%. The higher photo-induced cytotoxicity was due to the singlet oxygen ($^1O_2$) generated by

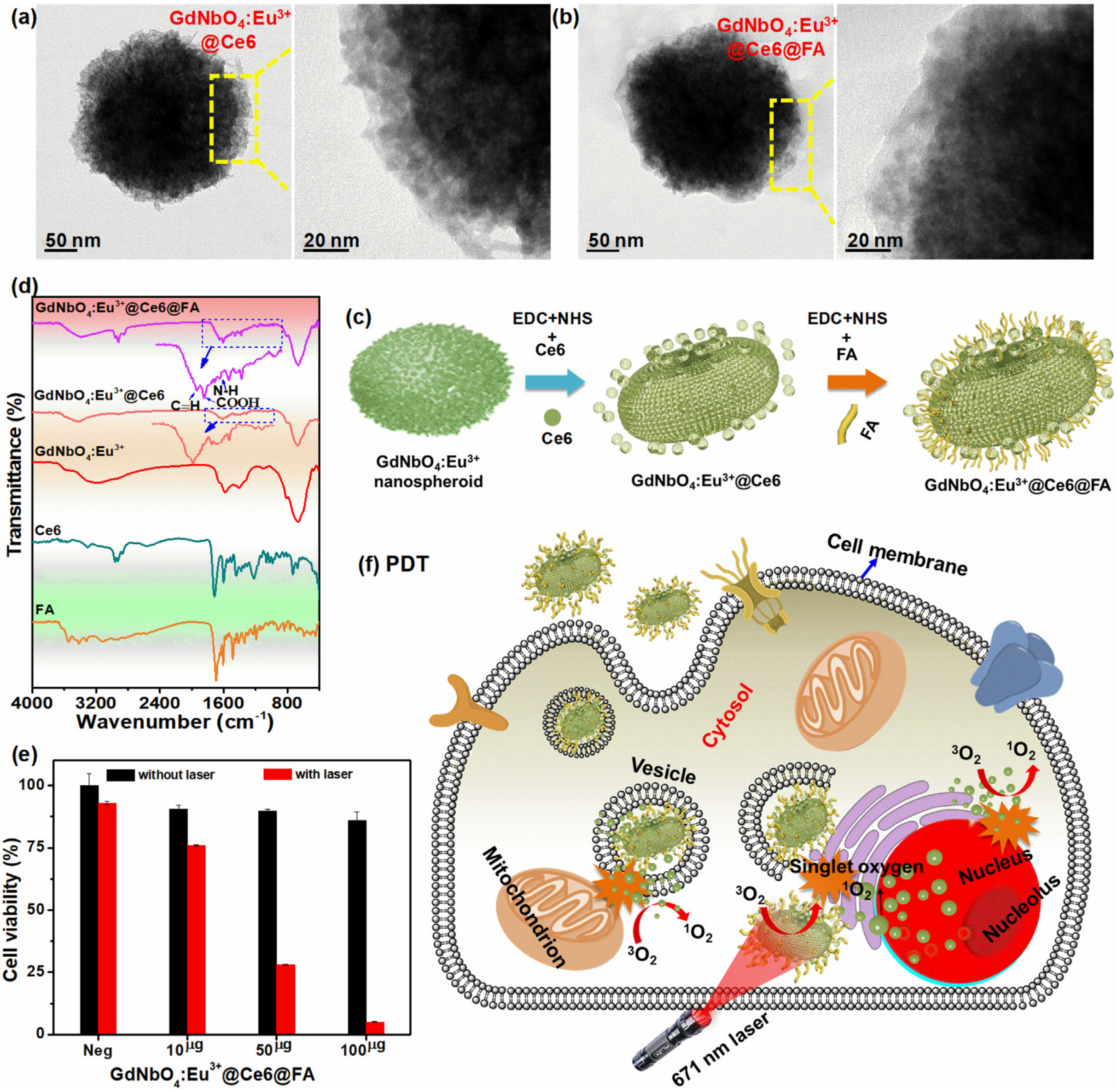

Fig. 7. (a) TEM images of Ce6 conjugated GdNbO$_4$:Eu^{3+} nanospheroids, (b) TEM images of FA conjugated GdNbO$_4$:Eu^{3+}@Ce6 nanospheroids, (c) schematic of the Ce6 and FA conjugation process, (d) FTIR spectra of FA, Ce6, GdNbO$_4$:Eu^{3+}@Ce6, and GdNbO$_4$:Eu^{3+}@Ce6@FA, (e) XTT assays, and (f) PDT mechanisms.

the photosensitizer Ce6 from the GdNbO$_4$:Eu^{3+}@Ce6@FA nanospheroids. Based on the observed results, the PDT mechanism is illustrated in Fig. 7f. The PDT results confirmed that the mesoporous GdNbO4:Eu^{3+} nanospheroids are promising carriers of photosensitizers in PDT. Therefore, the pre-ouzo effect induced mesoporous GdNbO4:Eu^{3+} nanospheroids could be potential theragnostic agents for integrated cancer diagnosis and therapy.

4. Conclusion

The successful synthesis of mesoporous GdNbO$_4$:Eu^{3+} nanospheroids by the self-assembly of GdNbO$_4$:Eu^{3+} nanodomains with simultaneous surface functionalization via a pre-ouzo effect induced hydrothermal reaction process was reported. The XRD patterns confirmed that the nanospheroids had a fergusonite structure. The formation of the surfactant-free micelles, the simultaneous complexation and capping effect of EDTA, and micelle-mediated self-assembly of the nanodomains were investigated by varying synthesis parameters, including the ratio of co-solvents, the concentration of EDTA, the reaction temperature, and the reaction time. FTIR spectra revealed that the surface of the GdNbO$_4$ and GdNbO$_4$:Eu^{3+} nanospheroids were functionalized with −OH, −CO and −COO functional groups, which enhanced their colloidal stability. The Raman spectrum displayed the characteristic vibrational modes of the GdNbO$_4$ nanospheroids and confirmed the existence of GdNbO$_4$ nanodomains within the mesoporous GdNbO$_4$ nanospheroids. When nanodomains were excited with a 346 nm wavelength, the mesoporous GdNbO$_4$ nanospheroids exhibited strong emissions in the visible region. The broadband excitation facilitated the energy transfer from the NbO$_6$ octahedra to the Eu^{3+} ions in the GdNbO$_4$ host lattice, which enhanced the red emission intensity under UV, NUV, and visible excitations. Magnetic measurements confirmed their paramagnetic nature, and FACS analysis established the high cellular internalization of the synthesized nanospheroids in HCT116 and SW680 colon cancer cells. This result was further confirmed with confocal microscope images, which displayed intense red emission from both the cytoplasm and nucleoplasm. The GdNbO$_4$ and GdNbO$_4$:Eu^{3+} nanospheroids also produced high contrast T1 MRI. PDT analysis subsequently confirmed that the mesoporous GdNbO$_4$:Eu^{3+} nanospheroids are potential carriers of photosensitizers. In conclusion, the obtained results suggest that mesoporous GdNbO$_4$:Eu^{3+}

nanospheroids are promising nanoprobes for multimodal bioimaging and PDT.

Declaration of Competing Interest

The authors declare that they have no known competing financial interests or personal relationships that could have appeared to influence the work reported in this paper.

Acknowledgements

We acknowledge financial support from the Basic Science Research Program through the National Research Foundation of Korea (NRF) funded by the Ministry of Science, ICT & Future Planning (2018R1D1A1B07050029, 2017M2A2A6A01020938, and 2014R1A5A1009799).

Appendix A. Supplementary material

Supplementary data to this article can be found online at https://doi.org/10.1016/j.apsusc.2019.144584.

References

[1] M.J. Schnermann, Organic dyes for deep bioimaging, Nature 551 (2017) 176.
[2] K.Y. Zhang, Q. Yu, H. Wei, S. Liu, Q. Zhao, W. Huang, Long-lived emissive probes for time-resolved photoluminescence bioimaging and biosensing, Chem. Rev. 118 (2018) 1770–1839.
[3] H. Ting, N. Na, C. Zhijun, L. Shujun, L. Shouxin, L. Jian, Novel quercetin aggregation-induced emission luminogen (AIEgen) with excited-state intramolecular proton transfer for in vivo bioimaging, Adv. Funct. Mater. 28 (2018) 1706196.
[4] C. Truillet, J.T. Cunningham, M.F.L. Parker, L.T. Huynh, C.S. Conn, D. Ruggero, J.S. Lewis, M.J. Evans, Noninvasive measurement of mTORC1 signaling with ^{89}Zr-Transferrin, Clin. Cancer Res. 23 (2017) 3045–3052.
[5] A.E. Hansen, A.L. Petersen, J.R. Henriksen, B. Boerresen, P. Rasmussen, D.R. Elema, P.M.A. Rosenschöld, A.T. Kristensen, A. Kjær, T.L. Andresen, Positron emission tomography based elucidation of the enhanced permeability and retention effect in dogs with cancer using copper-64 liposomes, ACS Nano 9 (2015) 6985–6995.
[6] D. Ni, J. Zhang, J. Wang, P. Hu, Y. Jin, Z. Tang, Z. Yao, W. Bu, J. Shi, Oxygen vacancy enables markedly enhanced magnetic resonance imaging-guided photothermal therapy of a Gd^{3+}-doped contrast agent, ACS Nano 11 (2017) 4256–4264.
[7] S. Kim, G. Yun, S. Khan, J. Kim, J. Murray, Y.M. Lee, W.J. Kim, G. Lee, S. Kim, D. Shetty, J.H. Kang, J.Y. Kim, K.M. Park, K. Kim, Cucurbit[6]uril-based polymer nanocapsules as a non-covalent and modular bioimaging platform for multimodal in vivo imaging, Mater. Horiz. 4 (2017) 450–455.
[8] J. Shi, X. Sun, S. Zheng, J. Li, X. Fu, H. Zhang, A new near-infrared persistent luminescence nanoparticle as a multifunctional nanoplatform for multimodal imaging and cancer therapy, Biomaterials 152 (2018) 15–23.
[9] Z. Xue, Z. Yi, X. Li, Y. Li, M. Jiang, H. Liu, S. Zeng, Upconversion optical/magnetic resonance imaging-guided small tumor detection and in vivo tri-modal bioimaging based on high-performance luminescent nanorods, Biomaterials 115 (2017) 90–103.
[10] W. Sheng, L. Jing, W. Zhantong, Z. Zijian, B. Ruiliang, L. Nan, L. Yijing, F. Xiao, J. Orit, F. Wenpei, Q. Junle, C. Siping, W. Tianfu, H. Peng, C. Xiaoyuan, Core–satellite polydopamine–gadolinium-metallofullerene nanotheranostics for multimodal imaging guided combination cancer therapy, Adv. Mater. 29 (2017) 1701013.
[11] J. Reguera, D. Jimenez de Aberasturi, M. Henriksen-Lacey, J. Langer, A. Espinosa, B. Szczupak, C. Wilhelm, L.M. Liz-Marzan, Janus plasmonic-magnetic gold-iron oxide nanoparticles as contrast agents for multimodal imaging, Nanoscale 9 (2017) 9467–9480.
[12] Y.-K. Peng, S.C.E. Tsang, P.-T. Chou, Chemical design of nanoprobes for T1-weighted magnetic resonance imaging, Mater. Today 19 (2016) 336–348.
[13] Q. Liu, Y. Sun, C. Li, J. Zhou, C. Li, T. Yang, X. Zhang, T. Yi, D. Wu, F. Li, 18F-labeled magnetic-upconversion nanophosphors via rare-earth cation-assisted ligand assembly, ACS Nano 5 (2011) 3146–3157.
[14] J. Zhou, X. Zhu, M. Chen, Y. Sun, F. Li, Water-stable NaLuF$_4$-based upconversion nanophosphors with long-term validity for multimodal lymphatic imaging, Biomaterials 33 (2012) 6201–6210.
[15] J. Yin, C. Li, D. Chen, J. Yang, H. Liu, W. Hu, Y. Shao, Structure and dysprosium dopant engineering of gadolinium oxide nanoparticles for enhanced dual-modal magnetic resonance and fluorescence imaging, Phys. Chem. Chem. Phys. 19 (2017) 5366–5376.
[16] R. Kumar, M. Nyk, T.Y. Ohulchanskyy, C.A. Flask, P.N. Prasad, Combined optical and MR bioimaging using rare earth ion doped NaYF4 nanocrystals, Adv. Funct. Mater. 19 (2009) 853–859.
[17] A. Saha, S.C. Mohanta, K. Deka, P. Deb, P.S. Devi, Surface-engineered multifunctional Eu:Gd$_2$O$_3$ nanoplates for targeted and pH-responsive drug delivery and imaging applications, ACS Appl. Mater. Interfaces 9 (2017) 4126–4141.
[18] L. Dong, P. Zhang, P. Lei, S. Song, X. Xu, K. Du, J. Feng, H. Zhang, PEGylated GdF$_3$:Fe nanoparticles as multimodal T1/T2-weighted MRI and X-ray CT imaging contrast agents, ACS Appl. Mater. Interfaces 9 (2017) 20426–20434.
[19] G.K. Das, Y. Zhang, L. D'Silva, P. Padmanabhan, B.C. Heng, J.S. Chye Loo, S.T. Selvan, K.K. Bhakoo, T.T. Yang Tan, Single-phase Dy$_2$O$_3$:Tb^{3+} nanocrystals as dual-modal contrast agent for high field magnetic resonance and optical imaging, Chem. Mater. 23 (2011) 2439–2446.
[20] Y. Liu, K. Ai, Q. Yuan, L. Lu, Fluorescence-enhanced gadolinium-doped zinc oxide quantum dots for magnetic resonance and fluorescence imaging, Biomaterials 32 (2011) 1185–1192.
[21] C. Feng, B. Wenbo, Z. Shengjian, L. Jianan, F. Wenpei, Z. Liangping, P. Weijun, S. Jianlin, Gd^{3+}-ion-doped upconversion nanoprobes: relaxivity mechanism probing and sensitivity optimization, Adv. Funct. Mater. 23 (2013) 298–307.
[22] L. Sudheendra, G.K. Das, C. Li, D. Stark, J. Cena, S. Cherry, I.M. Kennedy, NaGdF$_4$:Eu^{3+} nanoparticles for enhanced X-ray excited optical imaging, Chem. Mater. 26 (2014) 1881–1888.
[23] N. Luo, C. Yang, X. Tian, J. Xiao, J. Liu, F. Chen, D. Zhang, D. Xu, Y. Zhang, G. Yang, D. Chen, L. Li, A general top-down approach to synthesize rare earth doped-Gd$_2$O$_3$ nanocrystals as dualmodal contrast agents, J. Mater. Chem. B 2 (2014) 5891–5897.
[24] D. Ma, L. Meng, Y. Chen, M. Hu, Y. Chen, C. Huang, J. Shang, R. Wang, Y. Guo, J. Yang, NaGdF$_4$:Yb^{3+}/Er^{3+}@NaGdF$_4$:Nd^{3+}@sodium-gluconate: Multifunctional and biocompatible ultrasmall core–shell nanohybrids for ucl/mr/ct multimodal imaging, ACS Appl. Mater. Interfaces 7 (2015) 16257–16265.
[25] M. Ahrén, L. Selegård, A. Klasson, F. Söderlind, N. Abrikossova, C. Skoglund, T. Bengtsson, M. Engström, P.-O. Käll, K. Uvdal, Synthesis and characterization of PEGylated Gd$_2$O$_3$ nanoparticles for MRI contrast enhancement, Langmuir 26 (2010) 5753–5762.
[26] L. Bei, L. Chunxia, Y. Piaoping, H. Zhiyao, L. Jun, 808-nm-light-excited lanthanide-doped nanoparticles: rational design, luminescence control and theranostic applications, Adv. Mater. 29 (2017) 1605434.
[27] A. Saha, P.S. Devi, Surface functionalized multifunctional Gd$_2$O$_3$–fluorescein composite nanorods for redox responsive drug delivery and imaging applications, ACS Appl. Nano Mater. 1 (2018) 2898–2911.
[28] Y. Shen, A.J. Shuhendler, D. Ye, J.-J. Xu, H.-Y. Chen, Two-photon excitation nanoparticles for photodynamic therapy, Chem. Soc. Rev. 45 (2016) 6725–6741.
[29] X. Liu, C. Chen, S. Li, Y. Dai, H. Guo, X. Tang, Y. Xie, L. Yan, Host-sensitized and tunable luminescence of GdNbO$_4$:Ln^{3+} (Ln^{3+} = Eu^{3+}/Tb^{3+}/Tm^{3+}) nanocrystalline phosphors with abundant color, Inorg. Chem. 55 (2016) 10383–10396.
[30] M. Yang, X. Zhao, Y. Ji, F. Liu, W. Liu, J. Sun, X. Liu, Hydrothermal approach and luminescent properties for the synthesis of orthoniobates GdNbO$_4$:Ln^{3+} (Ln = Dy, Eu) single crystals under high-temperature high-pressure conditions, New J. Chem. 38 (2014) 4249–4257.
[31] J. Hou, R. Zhou, J. Zhang, Z. Wang, Z. Zhang, Z. Ding, Pressure and temperature study on the structural stability of GdNbO4:Eu3+, J. Phys. Chem. C 121 (2017) 14787–14794.
[32] Y. Zhao, J. Liu, Z. Chen, X. Zhu, M. Möller, Hybrid nanostructured particles via surfactant-free double miniemulsion polymerization, Nat. Commun. 9 (2018) 1918.
[33] A.B. Vysakh, K.J. Shebin, R. Jain, P. Sumanta, C.S. Gopinath, C.P. Vinod, Surfactant free synthesis of Au@Ni core-shell nanochains in aqueous medium as efficient transfer hydrogenation catalyst, Appl. Catal. B 575 (2019) 93–100.
[34] J. Xiong, J. Yu, Y. Zhang, W. Xia, S. Hu, Y. Zhang, J. Yang, One-step surfactant-free synthesis of KSc$_2$F$_7$ microcrystals: controllable phases, rich morphologies and multicolor down conversion luminescence properties, Cryst. Eng. Comm. 20 (2018) 3978–3986.
[35] X. Wang, Y. Ma, A. Sugunan, J. Qin, M.S. Toprak, B. Zhu, M. Muhammed, Synthesis of uniform quasi-octahedral CeO$_2$ mesocrystals via a surfactant-free route, J. Nanopart. Res. 13 (2011) 5879–5885.
[36] M.S. Akhtar, S. Riaz, R.F. Mehmood, K.S. Ahmad, Y. Alghamdi, M.A. Malik, S. Naseem, Surfactant and template free synthesis of porous ZnS nanoparticles, Mater. Chem. Phys. 189 (2017) 28–34.
[37] N. Pinna, M. Niederberger, Surfactant-free nonaqueous synthesis of metal oxide nanostructures, Angew. Chem. 47 (2008) 5292–5304.
[38] L. Baù, B. Bártová, M. Arduini, F. Mancin, Surfactant-free synthesis of mesoporous and hollow silica nanoparticles with an inorganic template, Chem. Commun. (2009) 7584–7586.
[39] A.T. Miah, S.K. Bharadwaj, P. Saikia, Surfactant free synthesis of gold nanoparticles within meso-channels of non-functionalized SBA-15 for its promising catalytic activity, Powder Technol. 315 (2017) 147–156.
[40] Y. Jiang, W. Sun, L. Zhou, L. Ma, Y. He, J. Gao, Improved performance of lipase immobilized on tannic acid-templated mesoporous silica nanoparticles, Appl. Biochem. Biotechnol. 179 (2016) 1155–1169.
[41] T.N. Zemb, M. Klossek, T. Lopian, J. Marcus, S. Schöettl, D. Horinek, S.F. Prevost, D. Touraud, O. Diat, S. Marčelja, W. Kunz, How to explain microemulsions formed by solvent mixtures without conventional surfactants, Proc. Natl. Acad. Sci. USA 113 (2016) 4260–4265.
[42] O. Diat, M.L. Klossek, D. Touraud, B. Deme, I. Grillo, W. Kunz, T. Zemb, Octanol-rich and water-rich domains in dynamic equilibrium in the pre-ouzo region of ternary systems containing a hydrotrope, J. Appl. Crystallogr. 46 (2013) 1665–1669.
[43] S. Schöttl, D. Touraud, W. Kunz, T. Zemb, D. Horinek, Consistent definitions of "the interface" in surfactant-free micellar aggregates, Colloids Surf. A 480 (2015) 222–227.
[44] S. Liu, P. Cool, O. Collart, P. Van Der Voort, E.F. Vansant, O.I. Lebedev, G. Van Tendeloo, M. Jiang, The influence of the alcohol concentration on the structural ordering of mesoporous silica: Cosurfactant versus cosolvent, J. Phys. Chem. B 107

(2003) 10405–10411.

[45] S. Song, C. Peng, Viscosities of binary and ternary mixtures of water, alcohol, acetone, and hexane, J. Dispersion Sci. Technol. 29 (2008) 1367–1372.

[46] S. Nihonyanagi, S. Yamaguchi, T. Tahara, Water hydrogen bond structure near highly charged interfaces is not like ice, J. Am. Chem. Soc. 132 (2010) 6867–6869.

[47] K. Sing, D. Everett, R. Haul, L. Moscou, R. Pierotti, J. Rouquerol, T. Siemieniewska, Physical and biophysical chemistry division commission on colloid and surface chemistry including catalysis, Pure Appl. Chem. 57 (1985) 603–619.

[48] M. Hirano, K. Ishikawa, Concentration dependence of luminescence properties of $GdNbO_4$:Er^{3+}/Yb^{3+} synthesized through hydrothermal route, J. Alloy. Compd. 709 (2017) 64–71.

[49] M. Yang, X. Liu, T. Hou, L. Du, Q. Wang, B. Chang, B. Li, J. Liu, G. Deng, I.V. Kityk, Synthesis and luminescent properties of $GdNbO_4$:Bi^{3+} phosphors via high temperature high pressure, J. Alloy. Compd. 723 (2017) 1–8.

[50] G. Blasse, L.G.J. De Haart, The nature of the luminescence of niobates $MNbo_3$ (M = Li, Na, K), Mater. Chem. Phys. 14 (1986) 481–484.

[51] K. Fulle, C.D. McMillen, L.D. Sanjeewa, J.W. Kolis, Hydrothermal chemistry and growth of fergusonite-type $RENbO_4$ (RE = La–Lu, Y) single crystals and new niobate hydroxides, Cryst. Growth Des. 16 (2016) 4910–4917.

[52] J. Lin, Z. Zhou, Q. Wang, Molten salt synthesis, characterization, and luminescence properties of $GdNbO_4$/$LuTaO_4$:Eu^{3+} phosphors, Mater. Res. Bull. 48 (2013) 2771–2775.

[53] G. Chen, T.Y. Ohulchanskyy, W.C. Law, H. Ågren, P.N. Prasad, Monodisperse $NaYbF_4$: Tm^{3+}/$NaGdF_4$ core/shell nanocrystals with near-infrared to near-infrared upconversion photoluminescence and magnetic resonance properties, Nanoscale 3 (2011) 2003–2008.

[54] Y.I. Park, J.H. Kim, K.T. Lee, K.-S. Jeon, H.B. Na, J.H. Yu, H.M. Kim, N. Lee, S.H. Choi, S.-I. Baik, H. Kim, S.P. Park, B.-J. Park, Y.W. Kim, S.H. Lee, S.-Y. Yoon, I.C. Song, W.K. Moon, Y.D. Suh, T. Hyeon, Nonblinking and nonbleaching upconverting nanoparticles as an optical imaging nanoprobe and T1 magnetic resonance imaging contrast agent, Adv. Mater. 21 (2009) 4467–4471.

[55] I.X. Cantarelli, M. Pedroni, F. Piccinelli, P. Marzola, F. Boschi, G. Conti, A. Sbarbati, P. Bernardi, E. Mosconi, L. Perbellini, L. Marongiu, M. Donini, S. Dusi, L. Sorace, C. Innocenti, E. Fantechi, C. Sangregorio, A. Speghini, Multifunctional nanoprobes based on upconverting lanthanide doped CaF_2: towards biocompatible materials for biomedical imaging, Biomater. Sci. 2 (2014) 1158–1171.